Mesoscale modelling of optical turbulence in the atmosphere: the need for ultrahigh vertical grid resolution

S. Basu [ORCID],[1]★ J. Osborn [ORCID],[2] P. He[3] and A. W. DeMarco[4]

[1] *Faculty of Civil Engineering and Geosciences, Delft University of Technology, 2628 CN Delft, the Netherlands*
[2] *Department of Physics, Centre for Advanced Instrumentation, Durham University, Durham, DH1 3LE, UK*
[3] *Department of Aerospace Engineering, University of Michigan, Ann Arbor, 48109 Michigan, USA*
[4] *United States Air Force, Washington D.C. 20330, USA*

ABSTRACT

The high-fidelity modelling of optical turbulence is critical to the design and operation of a new class of emerging highly sophisticated astronomical telescopes and adaptive optics instrumentation. In this study, we perform retrospective simulations of optical turbulence over the Hawaiian islands using a mesoscale model. The simulated results are validated against thermosonde data. We focus on turbulence in the free atmosphere, above the atmospheric boundary layer. The free atmosphere is particularly important for adaptive optics performance and for sky coverage calculations and hence has significant impact on performance optimization and scheduling of observations. We demonstrate that a vertical grid spacing of 100 m or finer is needed to faithfully capture the intrinsic variabilities of observed clear air turbulence. This is a particularly timely study because the next generation of extremely large telescopes are currently under construction and their associated suite of instruments are in the design phase. Knowledge of the expected accuracy of optical turbulence simulations and real-time forecasts will enable the design teams to (i) test and develop instrument designs and (ii) formulate operational procedure.

Key words: instabilities – turbulence – waves – atmospheric effects – methods: numerical.

1 INTRODUCTION

Most existing large telescopes and all future extremely large telescopes (ELTs) are investing in adaptive optics (AO) systems to correct for the time-variable and complex distortions caused by the Earth's atmosphere. The light from bright guide stars or laser beacons is used to sample the turbulence and a deformable mirror is shaped in real time to provide a diffraction limited and stable point spread function (PSF). However, several complexities combine to reduce the level of the correction, often resulting in a field-variable and partially corrected PSF. These factors include, among others, the spatial sampling of the wavefront sensors and the deformable mirrors, temporal sampling of the system, and angular separation from the guide stars.

The pursuit of better and more stable correction AO systems has become more sophisticated. Extreme AO systems are designed to have a higher spatial and temporal sampling to provide the very best on-axis performance. Such systems are ideally suited to imaging extra-solar planets and planet-forming discs (for example, Fusco et al. 2006; Macintosh et al. 2006).

In addition, other systems are designed to provide a uniform correction across a wide field of view. This is achieved by monitoring the wavefront in several directions at the same time and reconstructing the phase volume above the telescope. In this way, the optimal correction can be applied to one or more deformable mirrors to provide the best correction over a large field (see e.g.

Vidal, Gendron & Rousset 2010; Gendron et al. 2014; Martin et al. 2017).

The performance of all of these more sophisticated systems depends on the vertical distribution of optical turbulence (OT; commonly quantified by the refractive index structure parameter – C_n^2). For extreme AO, it has been shown that scintillation, caused by high-altitude turbulence can have a severe effect on the PSF symmetry of an AO-corrected coronagraphic system, significantly limiting the achievable contrast ratios (Cantalloube et al. 2018). In wide-field AO, tomographic reconstruction is used to control the AO system. This reconstructor matrix includes information on the vertical structure of the turbulence and must be updated at the same rate as the turbulence profile changes (Farley et al. 2020) to maintain optimal performance. The high-altitude turbulence is particularly important as this determines achievable sky-coverage of the system with strong high-altitude turbulence resulting in poorer and less uniform correction over the field.

Generally, knowledge of the vertical profiles of the OT strength and wind speeds is critical for AO operation and can be used for

(i) performance optimization of wide-field AO systems by updating the tomographic reconstructor as conditions change (Farley et al. 2020),
(ii) performance verification and monitoring of the complicated AO system (Gendron et al. 2014), and
(iii) post-processing of AO data (Beltramo-Martin et al. 2018).

The above applications are passive in that profiles taken by external profiling instruments, for example, the Multi-Aperture Scintillation sensor (Kornilov et al. 2007) or the Scintillation Distance and

★ E-mail: sukanta.basu@gmail.com
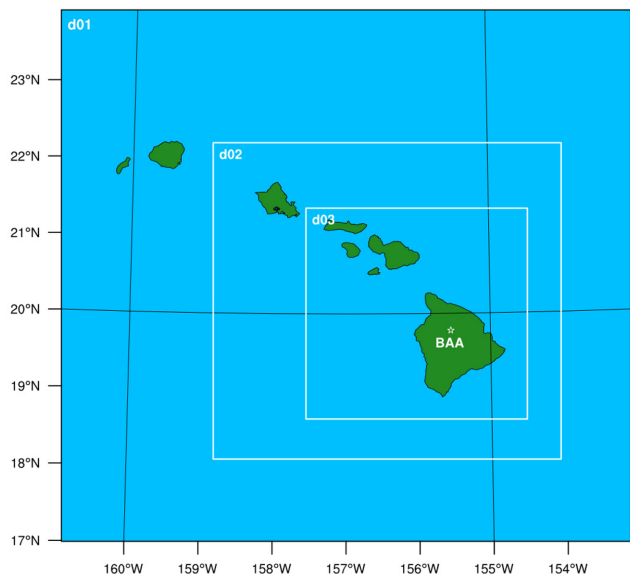
Figure 1. Illustration of the nested domain configuration for mesoscale modelling. The horizontal grid sizes for domains d01, d02, and d03 are 9, 3, and 1 km, respectively. The thermosonde launch site, near the Bradshaw Army Airfield (BAA), is demarcated by a white star.

Table 1. Summary of Simulations.

Simulation #	$\Delta_{x,y}$ (km)	N_z	Δ_z (m)	Δ_t (s)
R_1	9, 3, 1	51	variable	45, 15, 5
R_2	9, 3, 1	101	variable	45, 15, 5
R_3	9, 3, 1	286	~100 m	45, 15, 5
R_4	9, 3, 1	572	~50 m	30, 10, 2
R_5	9, 3, 1	927	~30 m	20, 5, 1

Note. For $\Delta_{x,y}$ and Δ_t, the three values separated by commas correspond to domains d01, d02, and d03, respectively.

Ranging technique (see e.g. Avila, Vernin & Masciadri 1997; Osborn et al. 2018), or from AO telemetry directly, where possible (Laidlaw et al. 2019), can be used to extract the relevant information.

However, if the vertical profile of the OT profile can be forecast in advance, then further gains can be expected:

(i) the tomographic reconstructor can be pre-computed – saving significant on-sky time (Laidlaw et al. 2019),

(ii) predictive control schemes can be pre-computed significantly reducing the temporal error (Juvenal et al. 2016), and

(iii) scheduling observations such that the most sensitive observations can be scheduled for the optimal time to maximize the probability of success (Masciadri, Lascaux & Fini 2013).

In this study, we demonstrate that high-fidelity simulations of OT is indeed feasible with state-of-the-art mesoscale models if one utilizes ultrahigh vertical grid resolution in conjunction with advanced physical parametrizations. Even though, we perform retrospective simulations, our model configurations are equally applicable for real-time forecasting applications. In other words, the proposed modelling framework can be utilized by AO teams to (i) test and develop instrument designs and (ii) formulate operational procedure.

The ELTs and instrument teams are currently in the process of finalizing their first-light instrument designs and operational plans. The work presented here is is therefore critical to feed into these plans and will influence the design and operation of these future systems.

In addition to the ELTs, many major observatories are transitioning to remote or service mode observing and therefore flexible queue scheduling to fit proposed observations to the prevailing conditions is becoming a reality. However, such facilities heavily rely on accurate and reliable OT forecasts. We believe that our proposed modelling framework will be able to deliver such OT forecasts.

2 MESOSCALE MODELLING

Bougeault et al. (1995) introduced the concept of mesoscale meteorological modelling to the optics community 25 yr ago. Since then, several research groups around the world (e.g. Masciadri, Vernin & Bougeault 1999; Cherubini et al. 2008; Frehlich et al. 2010; Giordano et al. 2014; He & Basu 2015) demonstrated its prowess in simulating and predicting optical turbulence. In the foreseeable future, the state-of-the-art mesoscale models are expected to play major roles in real-time operational forecasting of C_n^2 at various Very Large Telescope (VLT; e.g. the European Southern Observatory VLT) and ELT sites (see Masciadri et al. 2017, and the references therein).

2.1 Vertical grid resolution

With the ever-increasing availability of high-performance computing power, the OT modelling community has been utilizing finer and finer horizontal grid spacing ($\Delta_{x,y}$). Nowadays, it is no longer uncommon to use $\Delta_{x,y}$ of the order of 1 km or even sub-km in a mesoscale simulation. In contrast, the use of relatively coarse vertical grid spacing (Δ_z) is still very common in this community. To numerically discretize the lower part of the atmosphere (spanning from the surface to the lower stratosphere – approximately 20 to 30 km, where the OT strength diminishes in magnitude and is therefore not important here), most of the C_n^2 modelling studies (e.g. Giordano et al. 2014; Masciadri et al. 2017) use approximately 30–60 vertical levels (N_z). They use non-uniformly spaced vertical grid levels (aka grid stretching) to better resolve the atmospheric boundary layer (ABL) at the expense of poor grid spacing (say, $\Delta_z > 500$ m or coarser) in the free atmosphere (FA). The lowest part of our atmosphere, which feels the presence of the surface, is called the ABL. Over land and during the daytime, the height of the ABL could be around 1–3 km. In contrast, the nocturnal ABL height over land is rather shallow and rarely extends beyond 200–300 m. The atmospheric layer overlying the ABL is known as the FA.

It is a common knowledge that OT within the FA is typically much weaker than in the ABL. However, the FA is not completely quiescent. As a matter of fact, intermittent episodes of strong turbulent mixing, caused by various processes (e.g. gravity waves) and instabilities (e.g. Kelvin–Helmholtz instability), occur in the FA. Illustrative examples of such clear air turbulence (CAT) events over Cerro Tololo (Chile) and Dome C (Antarctic Plateau) were documented by Lawrence et al. (2004). Here, we demonstrate that ultrahigh vertical grid spacings ($\Delta_z < 100$ m or finer) are needed to faithfully simulate OT in the FA. In this context, an earlier conjecture from Cherubini et al. (2008) is worth noting:

'[...] high-altitude turbulence caused by free atmosphere shear (often associated with jet streams) or induced by the underlying complex terrain, can significantly affect the wave front phase de-correlation angle. Therefore, high-altitude turbulence also affects the corrected field of view of current-generation AO [adaptive optics] systems [...] and numerical prediction will benefit from increases in model vertical grid resolution aloft.'

We would like to highlight three papers that utilized ultrahigh vertical grid resolutions in atmospheric modelling and influenced
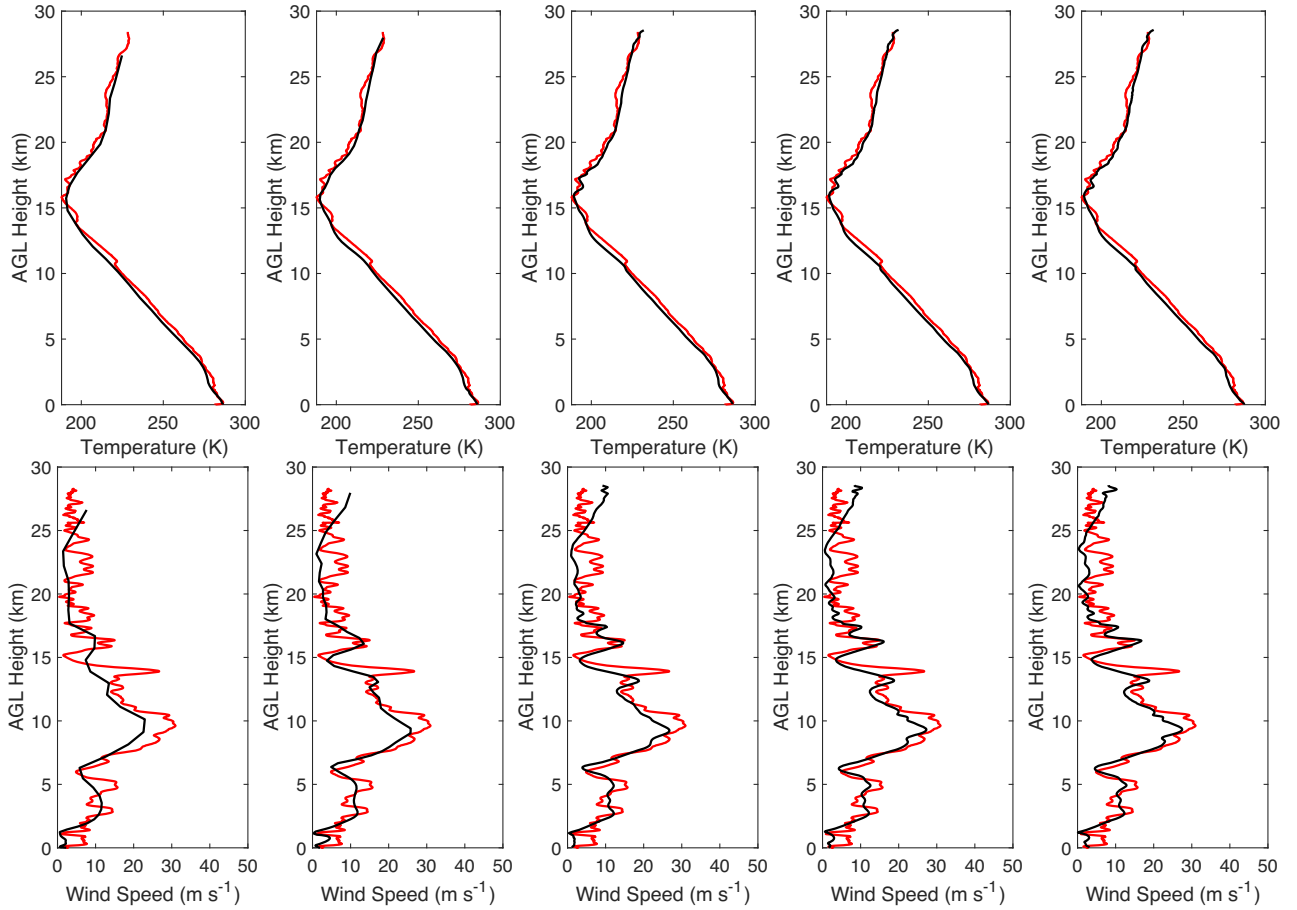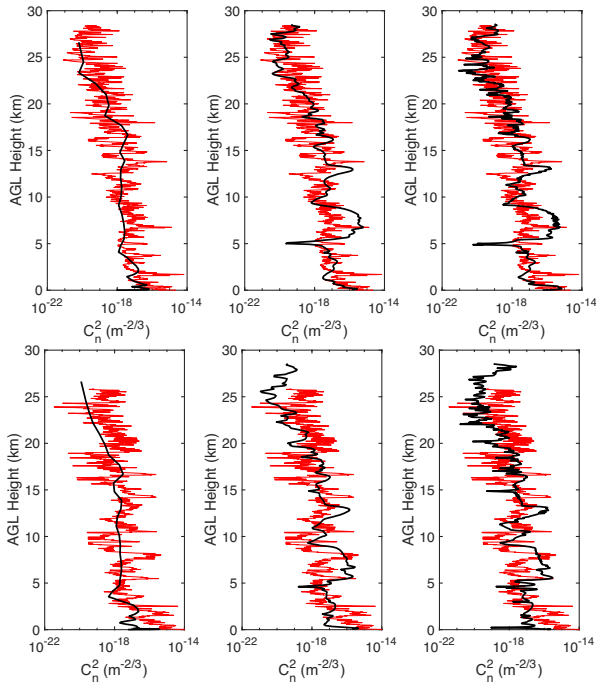
Figure 2. Comparison of measured (the red lines) and simulated (the black lines) profiles of temperature (top panels) and wind speed (bottom panels). From left to right, the panels correspond to simulations R_1, R_2, R_3, R_4, and R_5, respectively. Only the simulated profiles from the d03 domain ($\Delta_{x,y} = 1$ km) are shown. The thermosonde was launched at 9:43 UTC of 2002 December 12. The simulated profiles correspond to 9:50 UTC. The AGL elevations near the BAA site are reported in *y*-axes.
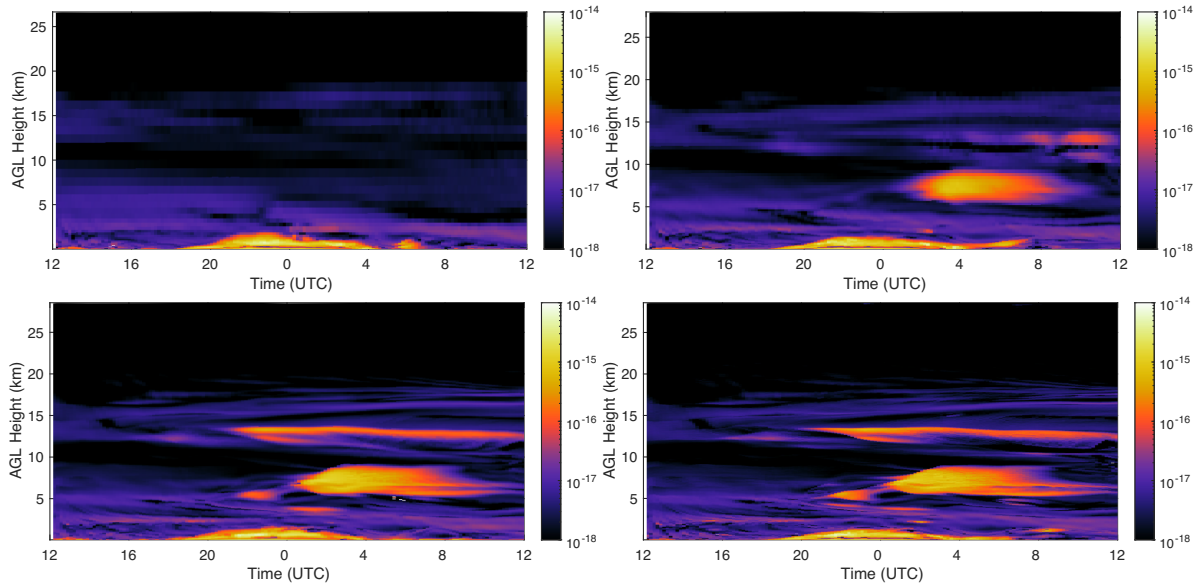
Figure 3. Time-height plots of simulated C_n^2 [unit: m$^{-2/3}$]. The top left-hand, top right-hand, bottom left-hand, and bottom right-hand panels correspond to simulations R_1, R_2, R_3, and R_5, respectively. Only the simulated profiles from the innermost domain (i.e. $\Delta_{x,y} = 1$ km) are shown. The *x*-axes range from 12 UTC of 2002 December 11 to 12 UTC of 2002 December 12. The AGL elevations near the BAA site are reported in *y*-axes.
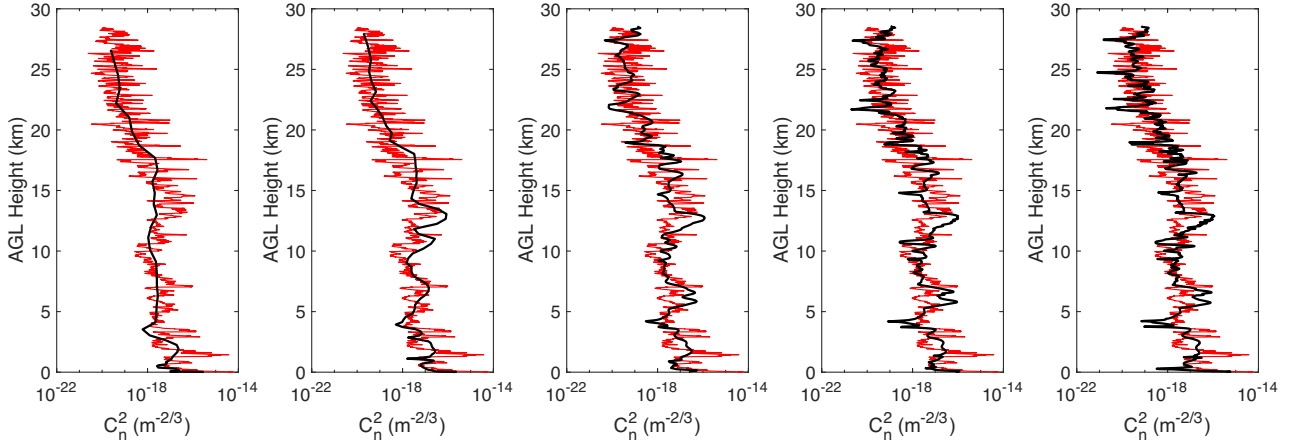
Figure 4. Comparison of measured (the red lines) and simulated (the black lines) C_n^2 profiles. From left to right, the panels correspond to simulations R_1, R_2, R_3, R_4, and R_5, respectively. Only the simulated profiles from the innermost domain (i.e. $\Delta_{x,y} = 1$ km) are shown. The thermosonde was launched at 9:43 UTC of 2002 December 12. The simulated profiles correspond to 9:50 UTC. The AGL elevations near the BAA site are reported in y-axes.

Figure 5. Comparison of measured (the red lines) and simulated (the black lines) C_n^2 profiles. The thermosondes were launched at 5:00 UTC (top panel) and 6:57 UTC (bottom panel) of 2002 December 12. From left to right, the panels represent results from the R_1, R_3, and R_5 simulations, respectively. Only the simulated profiles from the innermost domain (i.e. $\Delta_{x,y} = 1$ km) are shown.

our study. Mahalov & Moustaoui (2010) used a microscale model in conjunction with a rudimentary C_n^2 parametrization for OT simulations. Even though they were able to simulate OT layers that were modulated by wind shear and inertia–gravity waves, they did not quantify the sensitivities of their simulated results with respect to different Δ_z values. Furthermore, their study suffered from inadequate model validation against observational data. Masciadri et al. (2017) primarily used 62 vertical levels for OT simulations at Cerro Paranal. However, they also reported preliminary results from one simulation utilizing 173 vertical levels. They demonstrated that the simulation with higher vertical levels produce enhanced

variability in a simulated C_n^2 profile, although no validation was presented. In a more recent study, Skamarock et al. (2019) used a new-generation atmospheric model (called Model for Prediction Across Scales – MPAS) and investigated the impacts of Δ_z (100–800 m) on several meteorological variables (e.g. eddy diffusivity, Richardson number). However, this paper did not include any results pertaining to OT.

2.2 C_n^2 parametrization

Several kinds of C_n^2 parametrizations are currently utilized by the astronomy community (e.g. Trinquet & Vernin 2007), as well as the military organizations (e.g. Jumper et al. 2005). For example, Giordano et al. (2014) used an empirical relationship to estimate C_n^2 from mesoscale model-generated wind speed and temperature profiles. In contrast, Masciadri et al. (1999, 2013) used a physically based approach. In this study, we also utilize a physically based approach that was proposed by He & Basu (2015). Here, we summarize their approach for completeness.

The refractive index structure parameter (C_n^2) is related to the temperature structure parameter (C_T^2) via the Gladstone's relationship:

$$C_n^2 = (7.9 \times 10^{-5} P/T^2)^2 C_T^2, \tag{1}$$

where, P is the pressure and T is the temperature. Utilizing the Corrsin's expression (Corrsin 1951), one can estimate C_T^2 as follows:

$$C_T^2 = 3.2 \, (\overline{\varepsilon})^{-1/3} \, \overline{\chi}, \tag{2}$$

where, $\overline{\varepsilon}$ is the mean energy dissipation rate and $\overline{\chi}$ is the mean dissipation rate of temperature variance. Following Mellor & Yamada (1982), $\overline{\varepsilon}$ and $\overline{\chi}$ can be expressed as

$$\overline{\varepsilon} = \frac{(2\overline{e})^{3/2}}{B_1 L_M},$$

$$\overline{\chi} = \frac{(2\overline{e})^{1/2}}{B_2 L_M} \sigma_\theta^2, \tag{3}$$

where, $\overline{e}$ represents TKE and σ_θ^2 is the variance of potential temperature. L_M is the so-called master length-scale. Based on an extensive large-eddy simulation-based database, Nakanishi & Niino (2004, 2006) found the optimal values of the coefficients B_1 and B_2 to be equal to 24 and 15, respectively.

Table 2. Optical turbulence statistics calculated from the measured and simulated C_n^2 profiles.[*]

Profile	Time														
	0500 UTC					0657 UTC					0943 UTC				
	r_0	θ_{AO}	σ_I^2	d_B	d_K	r_0	θ_{AO}	σ_I^2	d_B	d_K	r_0	θ_{AO}	σ_I^2	d_B	d_K
Thermosonde	10.00	1.29	0.25	–	–	5.48	1.02	0.37	–	–	10.51	1.36	0.19	–	–
R_1-d03	35.92	3.32	0.04	0.10	1.27	34.90	3.52	0.04	0.10	0.64	37.14	3.38	0.04	0.14	1.10
R_5-d03	7.55	0.70	0.66	0.03	0.78	12.08	0.93	0.37	0.07	0.62	18.75	1.35	0.17	0.02	0.59

Note. [*]The symbols r_0, θ_{AO}, σ_I^2, d_B, and d_K refer to Fried parameter (cm), isoplanatic angle (arcsec), scintillation rate, Bhattacharyya distance, and (normalized) Kantorovich distance, respectively.
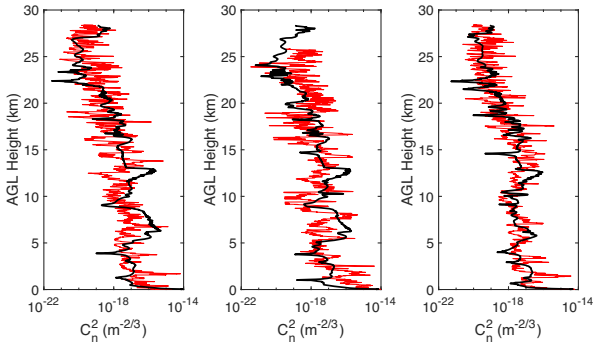
Figure 6. Comparison of measured (the red lines) and simulated (the black lines) C_n^2 profiles. The thermosondes were launched at 5:00 UTC (left-hand panel), 6:57 UTC (middle panel), and 9:43 UTC (right-hand panel) of 2002 December 12. Only the simulated profiles from the outermost domain (i.e. $\Delta_{x,y} = 9$ km) of R_5 simulation are shown.

The complexity of a turbulence closure is denoted by its hierarchical 'Level', a concept originally introduced by Mellor & Yamada (1974). The most elaborate formulation is a Level-4 closure scheme that requires numerical solution of 15 prognostic equations (Helfand & Labraga 1988). Given its prohibitive computational cost, this formulation has never been used in any operational mesoscale model. As a viable alternative, one can opt for a Level-3 closure since it typically involves four prognostic equations instead of 15. However, in our past research, we have sometimes found this formulation to be numerically unstable over complex terrain. Thus, in this study, we decided to use a Level-2.5 turbulence closure. In such a scheme, $\bar{e}$ is always obtained by solving a prognostic equation, whereas a diagnostic relationship is invoked to compute σ_θ^2. Please refer to Nakanishi & Niino (2004, 2006) for further technical details.

By combining equations (2) and (3), we get

$$C_T^2 = \frac{3.2 B_1^{1/3}}{B_2} (L_M)^{-2/3} \sigma_\theta^2. \tag{4}$$

In the surface layer, this equation is consistent with the Monin–Obukhov similarity theory. Furthermore, it is also in agreement with a well-known formulation of Tatarskii for FA (He & Basu 2015).

The master length-scale is composed of three different length-scales as follows (Nakanishi 2001; Nakanishi & Niino 2004):

$$\frac{1}{L_M} = \frac{1}{L_S} + \frac{1}{L_T} + \frac{1}{L_B}, \tag{5}$$

where, L_S, L_T, and L_B are the surface, the turbulence, and the buoyancy length-scales, respectively. Please refer to Nakanishi (2001) for the formulations of these length-scales. We would like to point out that Masciadri et al. (1999, 2013) use a single length-scale in their C_n^2 modelling. However, we believe that multiple length-scales are physically more meaningful as they can better represent various

layers of our atmosphere (e.g. surface layer, boundary layer, and FA) in mesoscale modelling.

2.3 Modelling configurations

We utilize the Weather Research and Forecasting (WRF) model (version 4.1.2) to simulate the dynamical evolution of OT over the Hawaiian islands. For the parametrization of atmospheric turbulence, the Level-2.5 scheme by Nakanishi & Niino (2004, 2006) is used; in the meteorology literature, it is widely known as the MYNN2 scheme. Based on the simulated turbulent variables (e.g. $\bar{e}$, σ_θ^2), C_n^2 is estimated following the approach of He & Basu (2015), as discussed in the previous section.

A one-way nested numerical modelling domain with three nested domains (d01–d03) is constructed (Fig. 1). In this type of multiscale nesting framework, lateral boundary conditions (LBCs) for d02 domain is provided by d01 domain; in turn, d02 domain imparts LBCs to d03. The horizontal grid spacings for d01, d02, and d03 are 9, 3, and 1 km, respectively. We run five different simulations (R_1–R_5) with varying vertical levels (refer to Table 1 for N_z values). The simulations R_1 and R_2 use non-uniform (stretched) vertical grid spacings, whereas the simulations R_3, R_4, and R_5 use uniform vertical grid spacings of 100, 50, and 30 m, respectively.[1] To satisfy the numerical stability requirements, the domains with smaller $\Delta_{x,y}$ values required smaller time-steps (Δ_t). On the same token, stringent time-steps were also needed for runs with higher N_z values. As a matter of fact, the computational cost of R_5 was approximately hundred times more than the cost of R_1.

All the simulations are run for a 24 h period: 12 UTC of 2002 December 11–12 UTC of 2002 December 12. For initialization and boundary conditions, the ERA5 reanalysis dataset is used. For validation of the simulated results, we use the thermosonde data collected during the Hawaii 2002 campaign (McHugh et al. 2008a; McHugh, Jumper & Chun 2008b). The thermosondes were launched from the Bradshaw Army Airfield (BAA; 19° 47' N, 155° 33' W); the location is marked with a white star on Fig. 1. The elevation of the BAA site is 1886 m from the mean sea level (MSL). Please note that for north-easterly flows, the airfield lies in the lee side of Mauna Kea (4207 m MSL) and experiences significant wake turbulence.

The thermosondes are suspended from ascending meteorological balloons (commonly known as radiosondes). They measure temperature, pressure, himidity, wind speed, and wind directions. In addition, thermosondes measure temperature difference over a horizontal distance of 1 m with a high sampling rate. By invoking the Kolmogorov–Obukhov–Corrsin hypothesis, C_T^2 values are computed

---

[1]Since the WRF model uses a pressure-based coordinate system, it is not possible to maintain a strictly uniform grid structure. Minute variations in Δ_z do occur during the simulations.
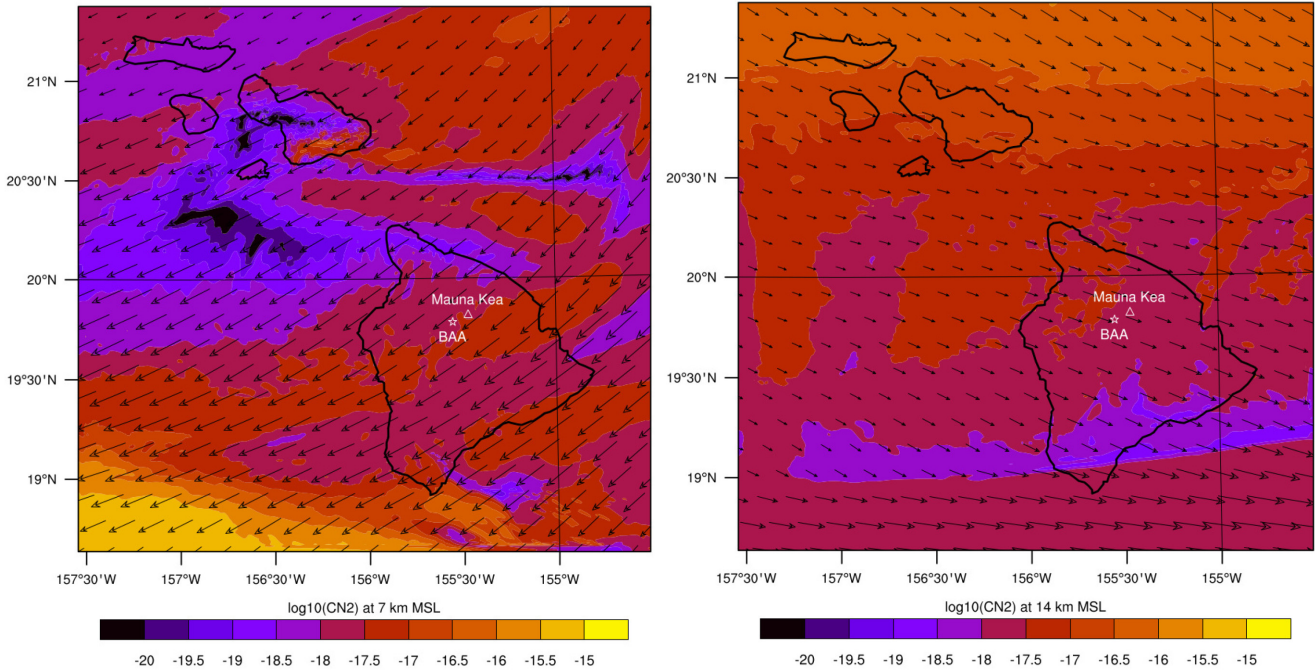
Figure 7. Contour plots of C_n^2 at the height of 7 km (left-hand panel) and 14 km (right-hand panel) above MSL. The overlaid arrows denote the velocity vectors at that height. The simulated data is from R_4 run and corresponds to 5 UTC of 2002 December 12. The thermosonde launch site and the Mauna Kea summit are demarcated by a white star and a white triangle, respectively.

from these temperature differences, and are subsequently converted to C_n^2 values. The vertical resolutions of the soundings are approximately 10–12 m. More technical details of thermosondes can be found in McHugh et al. (2008b) and Roadcap & Tracy (2009).

3 RESULTS

The measured and simulated temperature profiles are shown in the top panel of Fig. 2. The tropopause height is around 15 km above ground level (AGL). All the simulations capture the characteristics of the temperature profile (including the tropopause location) very accurately. The benefit of having higher vertical grid spacing is not obvious from this figure.

In the bottom panel of Fig. 2, the measured and simulated wind speed profiles are plotted. A jet stream is discernible around 10 km AGL. Clearly, with increasing vertical grid spacing, the agreement between the measured and simulated results improve significantly. The R_3–R_5 runs not only have captured the strength of the jet stream, they also have reproduced some of the oscillatory patterns.

The impact of vertical grid spacing is clearly visible in Fig. 3. The R_1 simulation, involving 51 vertical levels, does not generate any OT in the FA. However, other higher resolution simulations show significant amount of C_n^2 between 5-10 km AGL and also around 12 km AGL. These CAT patches are possibly produced due to the interactions of the jet stream with mountain waves (McHugh et al. 2008b).

In the OT modelling using the WRF model, the prognostic equations of turbulent kinetic energy and variance of temperature are solved in addition to the Navier–Stokes and scalar equations. These specific equations include several terms involving vertical gradients of velocity components and temperature. With finer Δ_z values, these gradients are computed with higher accuracy. In addition, the fidelity of the turbulent flux computations also greatly improves with finer

Δ_z. As a result of such improvements, the overall accuracy of simulated C_n^2 values increase significantly with enhanced vertical grid resolutions.

Measured and simulated profiles of C_n^2 corresponding to 9:43 UTC are shown in Fig. 4. The profile from the R_1 simulation is very smooth. In contrast, the R_5 simulation-based profile exhibits realistic, fine-scale fluctuations. Other simulations (i.e. R_2–R_4) portray intermediate traits.

For other validation times, the impact of vertical grid resolution remains the same as depicted in Fig. 5. The R_1 simulation performs rather poorly for both 5:00 UTC and 6:57 UTC. Significant improvement happens in R_3 case with $\Delta_z = 100$ m. Improvement from R_3 to R_5 is rather subtle.

Various OT statistics (e.g. Fried parameter) are computed based on the measured and simulations-based C_n^2 profiles in Table 2. The improvement from R_1 to R_5 is very significant for all the reported statistics.

In addition, the dissimilarities between the probability density functions (pdfs) of measured and simulated C_n^2 values are quantified by the Bhattacharyya distance (d_B) and (normalized) Kantorovich distance (d_K). Let us assume that there are p_i and q_i samples in the ith bin of the discretized pdfs of measured and simulated C_n^2, respectively. Then, the Bhattacharyya distance is simply defined as follows (Bhattacharyya 1943; Cha 2007):

$$d_B = -\log \left(\sum_i \sqrt{p_i q_i} \right). \qquad (6)$$

If p_i equals to q_i for every bin (i.e. the measured and simulated C_n^2 pdfs match perfectly), then d_B equals to zero. In other words, larger values of d_B signify more dissimilarities between the measured and simulated C_n^2 pdfs. The Kantorovich distance (d_K) was originally proposed by Kantorovich (1942, 1948) to address the so-called 'transportation problem', a special class of linear programming problems. The

definition of d_K and associated computational algorithm are rather involved and we refer the readers to a recent publication by Wang & Basu (2016) for details. Through idealized and realistic illustrations, Wang & Basu (2016) demonstrated the strengths of d_K over other commonly used statistics in OT research and advocated its usage for the validation of OT forecasts. Akin to d_B, smaller (larger) d_K values also indicate better (worse) forecasts. From Table 2, it is evident that with increasing N_z values, both the d_B and d_K values decrease significantly for the first (i.e. 0500 UTC) and the third (i.e. 0943 UTC) cases. However, the decrease was rather marginal for the second case (i.e. 0657 UTC).

In Fig. 6, simulated profiles from the outermost domain d01 (i.e. $\Delta_{x,y} = 9\,\mathrm{km}$) is compared against observations for the R_5 run. Interestingly, these simulated profiles are almost as good as the ones from the innermost domain d03 (i.e. $\Delta_{x,y} = 1\,\mathrm{km}$). Differences are primarily noticeable in the lowest 1 to 2 km. Thus, for the realistic simulation of turbulence in FA, vertical grid resolution seems to be much more important than the horizontal resolution.

During the period of interest, the wind was from north-west in the upper atmosphere (right-hand panel of Fig. 7). However, the predominant flow was north-easterly in the lower part of the atmosphere (left-hand panel of Fig. 7). Thus, the BAA site was in the wake of Mauna Kea for heights within the boundary layer. We believe that for such a complex flow situation, the horizontal grid spacing ($\Delta_{x,y}$) of 1 km is not sufficient. In our future work, we will utilize sub-km resolution in conjunction with grey-zone turbulence parametrizations to confront this challenging issue.

4 CONCLUSIONS

The vertical structure of OT severely impacts the performance of modern and sophisticated AO systems. For coronagraphic Extreme AO systems designed to give the ultimate correction on-axis, high-altitude turbulence leads to an asymmetry in the PSF. For wide-field AO, designed to provide a uniform correction over a wide-field, high-altitude turbulence limits the performance and the usable sky coverage.

In this study, we have examined the fidelity of a mesoscale model in simulating high-altitude turbulence. We found that vertical grid spacing of 100 m or finer is needed to faithfully capture the intrinsic variabilities of observed CAT. Currently, we are investigating the capability of our proposed modelling framework for other astronomical sites (e.g. Paranal in Chile). In addition, we are exploring its application in real-time forecasting by utilizing operational data from the Global Forecast System. These findings will be reported in a follow-up publication.

DATA AVAILABILITY

The WRF model-generated data are available from http://doi.org/10.5281/zenodo.3928133.

REFERENCES

Avila R., Vernin J., Masciadri E., 1997, Appl. Opt., 36, 7898
Beltramo-Martin O., Correia C. M., Neichel B., Fusco T., Ragland S., Wizinowich P. L., 2018, in Close L. M., Schreiber L., Schmidt D., eds, Proc. SPIE Conf. Ser. Vol. 10703, Adaptive Optics Systems VI. SPIE, Bellingham, p. 809
Bhattacharyya A., 1943, Bull. Calcutta Math. Soc., 35, 99
Bougeault P., De Hui C., Fleury B., Laurent J., 1995, Appl. Opt., 34, 3481
Cantalloube F. et al., 2018, A&A, 620, L10
Cha S.-H., 2007, Int. J. Math. Model Method Appl. Sci., 1, 300
Cherubini T., Businger S., Lyman R., Chun M., 2008, J. Appl. Meteorol. Climatol., 47, 1140
Corrsin S., 1951, J. Appl. Phys., 22, 469
Farley O. J. D., Osborn J., Morris T. J., Fusco T., Neichel B., Correia C., Wilson R. W., 2020, MNRAS, 494, 2773
Frehlich R., Sharman R., Vandenberghe F., Yu W., Liu Y., Knievel J., Jumper G., 2010, J. Appl. Meteorol. Climatol., 49, 1742
Fusco T. et al., 2006, Opt. Express, 14, 7515
Gendron E., Morel C., Osborn J., Martin O., Gratadour D., Vidal F., Le Louarn M., Rousset G., 2014, in Marchetti E., Close L. M., Véran J.-P., eds, Proc. SPIE Conf. Ser. Vol. 9148, Adaptive Optics Systems IV. SPIE, Bellingham, p. 91484N–13
Giordano C., Vernin J., Trinquet H., Muñoz-Tuñón C., 2014, MNRAS, 440, 1964
He P., Basu S., 2015, in Laser Communication and Propagation through the Atmosphere and Oceans IV, SPIE, San Diego. p. 96140K
Helfand H. M., Labraga J. C., 1988, J. Atmos. Sci., 45, 113
Jumper G. Y., Roadcap J. R., Adair S. C., Seeley G. P., Fairley G., 2005, J. Directed Energy, 1, 183
Juvenal R., Kulcsar C., Raynaud H.-F., Conan J.-M., 2016, in Marchetti E., Close L. M., Veran J.-P., eds, Proc. SPIE Conf. SER. Vol. 9909, Adaptive Optics Systems V. SPIE, Bellingham, p. 215
Kantorovich L. V., 2006, J. Math. Sci., 133, 1381
Kantorovich L. V., 2006, J. Math. Sci., 133, 1383
Kornilov V., Tokovinin A., Shatsky N., Voziakova O., Potanin S., Safonov B., 2007, MNRAS, 382, 1268
Laidlaw D. J. et al., 2019, MNRAS, 483, 4341
Lawrence J. S., Ashley M. C. B., Tokovinin A., Travouillon T., 2004, Nature, 431, 278
Macintosh B. et al., 2006, in Ellerbroek B. L., Calia D. B., eds, Proc. SPIE Conf. Ser. Vol. 6272, Advances in Adaptive Optics II. SPIE, Bellingham, p. 177
Mahalov A., Moustaoui M., 2010, Laser Photonics Rev., 4, 144
Martin O. A. et al., 2017, A&A, 598, A37
Masciadri E., Vernin J., Bougeault P., 1999, A&AS, 137, 185
Masciadri E., Lascaux F., Fini L., 2013, MNRAS, 436, 1968
Masciadri E., Lascaux F., Turchi A., Fini L., 2017, MNRAS, 466, 520
McHugh J. P., Dors I., Jumper G. Y., Roadcap J. R., Murphy E. A., Hahn D. C., 2008a, J. Geophys. Res., 113, D15123
McHugh J. P., Jumper G. Y., Chun M., 2008b, PASP, 120, 1318
Mellor G. L., Yamada T., 1974, J. Atmos. Sci., 31, 1791
Mellor G. L., Yamada T., 1982, Rev. Geophys., 20, 851
Nakanishi M., 2001, Boundary-Lay. Meteorol., 99, 349
Nakanishi M., Niino H., 2004, Boundary-Lay. Meteorol., 112, 1
Nakanishi M., Niino H., 2006, Boundary-Lay. Meteorol., 119, 397
Osborn J. et al., 2018, MNRAS, 478, 825
Roadcap J. R., Tracy P., 2009, Radio Science, 44, RS2011
Skamarock W. C., Snyder C., Klemp J. B., Park S.-H., 2019, Mon. Weather Rev., 147, 2641
Trinquet H., Vernin J., 2007, Environ. Fluid Mech., 7, 397
Vidal F., Gendron E., Rousset G., 2010, J. Opt. Soc. Am. A, 27, 253
Wang Y., Basu S., 2016, Opt. Lett., 41, 4008

This paper has been typeset from a TEX/LATEX file prepared by the author.